Near-surface characterization using Distributed Acoustic Sensing in an urban area: Granada, Spain

Yang Li[1], Mathieu Perton[2], Beatriz Gaite[3], Sandra Ruiz-Barajas[3], Zack J. Spica[1]

[1]Department of Earth and Environmental Sciences, University of Michigan, Ann Arbor, MI, USA.

[2]Instituto de Ingeniería, Universidad Nacional Autónoma de México, CDMX, Mexico.

[3]National Geographic Institute of Spain (IGN), Madrid, Spain.

Note: This is a non-peer reviewed preprint submitted to EarthArXiv. It has also been submitted to Geophysical Journal International for peer review and publication consideration. If it is accepted, the EarthArXiv will be appropriately updated to reflect its publication status.

Corresponding author: Zack Spica, zspica@umich.edu

Abstract

The Granada Basin in southeast Spain is an area of moderate seismicity. Yet, it hosts some of the highest seismic hazards in the Iberian Peninsula due to the presence of shallow soft sediments amplifying local ground motion. In urban areas, seismic measurements often suffer from sparse instrumentation. An enticing alternative to conventional seismometers is the Distributed Acoustic Sensing (DAS) technology that can convert fiber-optic telecommunication cables into dense arrays of seismic sensors. In this study, we perform a shallow structure analysis using the ambient seismic field interferometry method. We use a DAS array field test in the city of Granada obtained on the August 26^{th} and 27^{th}, 2020, using a telecommunication fiber. In addition to the existing limitations of using DAS with unknown fiber-ground coupling conditions, the complex geometry of the fiber and limited data recording duration further challenge the extraction of surface-wave information from the ambient seismic field in such an urban environment. Therefore, we develop an ad-hoc processing scheme in which we incorporate a frequency-wavenumber ($f-k$) filter to enhance the quality of the virtual shot gathers and related multi-mode dispersion images. We are able to employ this dataset to generate several shear-wave velocity (V_S) profiles for different sections of the cable. The shallow V_S structure shows a good agreement with different geological conditions of soil deposits. This study demonstrates that DAS could provide insights into soil characterization and seismic microzonation in urban areas. In addition, the results contribute to a better understanding of local site response to ground motion.

1 Introduction

The Granada basin, located in Andalusia in the southeast of Spain (Fig. 1), undergoes some of the highest seismic hazards in the Iberian Peninsula. The Spanish Seismic Code (NCSE-02, 2002) suggests that peak ground accelerations of 2.3 g are expected over a 500-years return period (J. P. Montilla et al., 2001; Sanz de Galdeano et al., 2003; J. A. P. Montilla et al., 2003). This remarkably strong ground motion for the region is due to a series of accumulating factors. In a regional context, Andalusia has a low-to-moderate seismicity resulting from the collision between the Eurasian and African plates (Grimison & Chen, 1986; Hamdache, 1998; Serrano et al., 2002). Small seismic events are frequent, and moderate magnitude earthquakes (e.g., $M_w \leq 5.5$) are rather unusual. Nonetheless, there are large earthquakes have been recorded: the 1910 M_w6.2 Adra earthquake (Stich et al., 2003), the deep 1954 M_w7.8 Durcal earthquake (Chung & Kanamori, 1976; Buforn et al., 1991), and the deep 2010 M_w6.2 Nigüelas earthquake (Buforn et al., 2011). At the local scale, the Granada Basin is surrounded by numerous faults, causing active microseismicity ($M_w \geq 3.5$) in the Iberian Peninsula (Muñoz et al., 2002; Morales et al., 1997; Lozano et al., 2022), but also catastrophic historical earthquakes: e.g., the 1884 December 25th Andalusian earthquake (M≈6.7-7.1) that occurred in the south of the Granada basin, near Alhama de Granada (Sánchez, 1987; Morales et al., 1996; Muñoz & Udias, 1992).

Besides, the seismic hazard in the basin is further exacerbated by the local site conditions, which can lead to significant amplification of seismic ground motion. In the past, site effects in this region have contributed to great damage during moderate and large earthquakes (Morales et al., 1991, 1993; García-García et al., 1996; Vidal & Castillo, 1994). Near-surface lithology can strongly increase the amplitude and duration of earthquake ground motion and can also respond non-linearly to incident seismic waves (Aki, 1998; Cruz-Atienza et al., 2016; Sanchez-Sesma, 1987; Viens et al., 2022). In particular, sedimentary basins with soft sediments over hard basement rocks are particularly prone to strong site effects as observed with the 1985 Michoacán earthquake in Mexico City (Campillo et al., 1989), the 1995 Kobe earthquake in Japan (Pitarka et al., 1998), and the 2015 Gorkha earthquake in Nepal (Galetzka et al., 2015), among others. For these reasons, site characterization is of great importance to seismic hazard analysis (Bommer et al., 2017; Aki, 1993), but generally challenging to obtain in densely populated areas. In urban centers, microzonation studies involving cabled or autonomous nodal acquisition are particularly onerous to conduct because of the physical, legal, and logistical constraints inherent to seismic experiments. In addition, seismic surveys are often expensive, preventing scientists and engineers from covering larges areas. In some singular cases, the energy industry may provide assistance, and collaborative efforts emerge (e.g., Castellanos & Clayton, 2021), as was the case for the Granada basin (Morales et al., 1990).

Today, an alternative to heavy seismic surveys called Distributed Acoustic Sensing (DAS) is emerging as a promising tool for urban microzonation (Dou et al., 2017; Z. J. Spica et al., 2020; Shragge et al., 2021). DAS is a rapidly evolving technology that converts standard telecommunication fiber-optic cables into large and ultra-dense seismic vibration sensing arrays. In its simplest form, a DAS interrogator is an optoelectrical unit probing a fiber with repeated laser pulses. A fraction of the light is reflected back to the interrogator due to optical heterogeneities. External forcing, such as seismic waves, generate phase shifts of the back-scattered Rayleigh light, which are measured by the interrogator and are proportional to the total strain (or strain rate) along the direction of the fiber and over a sliding spatial distance (i.e., the gauge length) (Grattan & Sun, 2000). For a review of the DAS technology, we refer the reader to Hartog (2017).

DAS offers new opportunities for urban microzonation by providing ultra-high measurements in areas that are sometimes difficult to probe. Millions of kilometers of fiber-optic cables have already been laid out around the world over the past decades to support our modern telecommunication infrastructures. Many of these cables are concentrated in urban centers and could therefore compensate for the scarcity of available seismic stations. In addition, while providing ultra-dense measurements, DAS interrogators can acquire data within a wider frequency range (from mHz to kHz) than standard exploration geophones (Lindsey, Rademacher, & Ajo-Franklin, 2020). Yet, there are also known trade-offs and drawbacks to consider when designing a DAS survey and setting up acquisition parameters (Z. J. Spica et al., 2023). For example, a larger gauge length will lower the spatial resolution and decrease statistical uncertainty in measurements over the gauges (E. R. Martin, 2018). Furthermore, the gauge length parameter affects the amplitude response by generating zero strain notches at harmonic frequencies (Jousset et al., 2018; Lindsey, Rademacher, & Ajo-Franklin, 2020). Except in special cases, DAS commonly has a lower signal-to-noise ratio (SNR) and a more limited angular sensitivity than standard geophones due to its broadside insensitivity to incoming waves with particle motions oblique to the fiber axis (E. R. Martin et al., 2018). Nonetheless, these limitations are often compensated by the fact that DAS can provide large aperture and dense sampling of the seismic wavefield using only one signal power source.

DAS for urban seismology has proven to be successful in monitoring earthquakes (Lindsey et al., 2017; Fang et al., 2020), tracking traffic signals (Lindsey, Yuan, et al., 2020; Yuan et al., 2020; E. R. Martin et al., 2018), identifying different types of noise sources (Huot et al., 2018; Zhu & Stensrud, 2019; X. Wang et al., 2020), monitoring the structural health of a wind turbine tower (Hubbard et al., 2021) and providing geotechnical information of the shallow subsurface (Z. J. Spica et al., 2020). In recent years, several studies focused on the near-surface characterization with DAS and ambient seismic field (ASF) interferometry (Dou et al., 2017; Parker et al., 2018; Z. J. Spica et al., 2020; Yang et al., 2022; Shragge et al., 2021; Viens et al., 2023; Jousset et al., 2018; Ajo-Franklin et al., 2019; Zeng et al., 2017; E. R. Martin et al., 2017; E. Martin et al., 2016; Lellouch et al., 2019).

ASF interferometry is particularly suitable for urban near-surface imaging because it is cost-effective, noninvasive, and does not require active sources. In addition, when using existing telecommunication infrastructure, researchers can get access to measurement sites that are normally difficult to reach or even impossible to access. However, applying ASF interferometry with DAS also comes with a series of practical and technical challenges that may prevent researchers from taking full advantage of the methods. First, because researchers are not included in the fiber network design process, they often have very limited inputs on the deployment condition (including fiber coupling with the ground) and the precise geometry of the cable. This frequently leads to practical constraints forcing researchers to trade-off between accurate but time-consuming fiber geolocation (Biondi et al., 2023) and matching channel locations utilizing the approximate mapping provided by the cable owner and the nominal channel spacing set during acquisition. Second, the broadside insensitivity to incoming waves recorded with DAS means that the wavefield energy not aligned with the cable will have a weaker contribution during the interferometry process (E. Martin et al., 2016; Shragge et al., 2021). Therefore, in the case of a complex fiber geometry, the interferometry can be limited to specific sections of the cable (Z. J. Spica et al., 2020). Third, the fiber/ground coupling condition may vary substantially along the cable. In some extreme cases, the cable can be fully uncoupled, preventing the use of some sections of the cable. In all cases, these issues must be taken into consideration prior to interpreting the data, and adapted data processing should address these issues to obtain reliable results.

In this study, we expose the benefits and challenges of using DAS for microzonation in a densely populated urban area. We present a case study in Granada using a 20-km section of an existing telecommunication fiber, which recorded ASF with a DAS interrogator for less than one day. We show that such a short data set can be used to infer the shallow velocity structure in several regions of the city. We first discuss the effect of data pre-processing on the retrieval of accurate dispersion images at high frequency. We then perform a multi-mode inversion to constrain the local 1-D shallow shear-wave velocity (V_S) structure. Finally, we further discuss the challenges of operating high-frequency ASF interferometry in an urban area with a limited amount of data and compare our results with previous studies to validate them.

2 Geological setting

The Granada basin is one of the largest intramountainous Neogene–Quaternary basins of the Betic Cordilleras (Morales et al., 1990; Banda & Ansorge, 1980), which resulted from the collision between the Eurasian and African plates between the Cretaceous and Neogene periods. Jurassic and Cretaceous carbonate sedimentary series bound the northern and western parts of the basin, while the southern and eastern regions are bordered with metamorphic units (García-Dueñas & Balanyá, 1986).

The Granada basin deep structure was first estimated through a combination of gravity data and seismic-reflection profiles (Morales et al., 1990; Rodríguez-Fernández & De Galdeano, 2006). These results highlight a complicated basin geometry with four deep micro-basins (i.e., depocen-

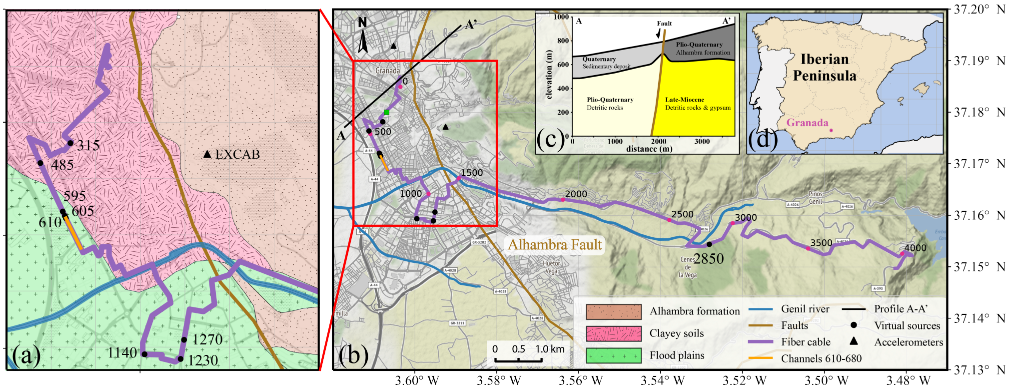

Figure 1. The GranaDAS array. (a) Map of the DAS fiber array located in the city of Granada. The background colors highlight the main superficial geological deposits (modified from Geological Survey of Spain, 2014). (b) The extent of the fiber probed during the experiment. The red box highlights the panel shown in (a). (c) Tectonic model derived from gravity data along profile A-A' shown in (b) (modified from Madarieta-Txurruka et al., 2021). (d) Map of Spain highlighting the location of Granada.

ters) with depths varying between ∼1800-3000 m. The complexity of the basin geometry was further evidenced through 3-D imaging of the V_S derived from Rayleigh wave dispersion analysis (Chourak et al., 2003). While the sedimentary layers in the basin have relatively low V_S velocities (Banda & Ansorge, 1980; Gurria et al., 1997; Serrano et al., 2002), the basement under the basin typically exhibits velocities around ∼3.1 km/s (Banda & Ansorge, 1980). According to the basement map of the Granada basin, the city of Granada lies on the edge of an 1800-m depocenter (Morales et al., 1990; Gil-Zepeda et al., 2002). One interpretation of gravity and seismic reflection data suggests that the depth of the basement beneath Granada city is approximately 1000 m (Morales et al., 1990), while another quantitative study of subsidence indicates a depth of 500-900 m under the urban areas (Rodríguez-Fernández & De Galdeano, 2006). As a result, the analysis of the shallow subsurface described in this contribution is unlikely to reach the interface with the Basin's basement. Overall, these studies contributed to show that the overall structure of the basin contributes to the seismic wave amplification (Gil-Zepeda et al., 2002; Lee et al., 2008). However, the lack of resolution in the shallow subsurface may lead to an underestimation of the wave amplifications (Semblat et al., 2005; Narayan & Singh, 2006), as shallow stratigraphy may impact local site effect's peak amplitude and frequency, and the dispersion behavior of surface waves (e.g., Cruz-Atienza et al., 2016; Brissaud et al., 2020; Lee et al., 2008).

As such, the shallow basin structure has been assessed sporadically in Granada (Navarro et al., 2010; Vidal et al., 2014). Navarro et al. (2010) got six shallow (∼40 m depth) V_S models throughout the city by means of inversion of Rayleigh wave dispersion curves obtained through the SPAC method. Vidal et al. (2014) obtained ten V_S models following a joint inversion of Rayleigh wave dispersion curves and horizontal-to-vertical spectral ratio from microtremor. They showed that the average V_S for the upper 30 m of soil (V_{S30}) varies from $\sim$300 m/s to $\sim$520 m/s, coinciding with the Genil river deposit and Alhambra formation, respectively.

In Granada, we can distinguish two main shallow geological formations (Fig. 1c). In the western part of the Alhambra fault, we observe Quaternary sediments characterized by alluvial facies. They are overlaid by a thin layer of clayey soils and flood plains (Fig. 1a), formed by recent sedimentary deposits of Holocene ages as a product of the Genil river draining. In the eastern part, near the hill zones, we observe the Alhambra formation, which is characterized by sands, gravel, and carbonate conglomerates of Pliocene ages. Both the Alhambra formation and Granada depocenter shallow sedimentary deposits have a similar thickness ($\sim$200 m) near the Granada fault zone (Madarieta-Txurruka et al., 2021).

3 Data and methods

3.1 The GranaDAS array

The fiber-optic cable used in this study is operated by the IRAM (*Instituto de Radioastronomía Milimétrica*) and provides continuous telecommunication between the radio-telescope at the top of the Sierra Nevada and its headquarters in Granada (Fig. 1). The cable has no extra fiber (i.e., dark) available during normal operation. Therefore, we connected a Febus Optics A1-R interrogator to the fiber during the maintenance of the radio-telescope that happened between the 26^{th} and 27^{th} of August 2020. In total, we collected about 19 hours of strain rate data at a sampling rate of 2000 Hz. Apart from the night interruption, during which the radio-telescope was operating, the setup recorded data along the first 20 km of the fiber from the observatory, with 4167 channels spaced by 4.8 m, and with a 9.6-m gauge length. The raw dataset has a volume of up to 4.56 TB.

The GranaDAS array crosses different neighborhoods in Granada before climbing up the Sierra Nevada in the east (Fig. 1). The fiber installation report provides a detailed location of the fiber, which is most often located underneath the side of the roads. The report does not mention any fiber slack loops placed in manholes, suggesting the fiber is outstretched between the IRAM and the radio-telescope. Therefore, the location of each channel has been interpolated based on the recording parameters, leaving a moderate degree of uncertainty in the assigned channel geolocations. Besides, the coupling conditions of the fiber with the ground are unknown. In addition, there are two three-component accelerometers in the city that are managed by the National Geographic Institute of Spain.

3.2 Ambient seismic field interferometry

In an urban environment, ambient seismic sources are generally strongly localized, moving, narrow band, or even monochromatic (Jakkampudi et al., 2020; Bonnefoy-Claudet et al., 2006). For example, these sources can originate from different traffic levels along the roads, the presence of cooling and heating systems throughout the neighborhoods, construction activities, or even the presence of pedestrians and bicycles near the fiber. All these sources make the assumption of an equipartitioned ASF unrealistic (e.g., Snieder et al., 2010). Spectral and time normalizations (Bensen et al., 2007) are generally unable to counterbalance the resulting heterogeneous illumination. Additionally, spurious arrivals can appear in the cross-correlation functions (CCFs) when the sources are between the receivers (Retailleau & Beroza, 2021). The specific case of DAS with a shallow fiber placed along the road lines in a city is thus challenging for obtaining reliable CCFs. As previously mentioned, the measurements have been made only during day time, so quiet night hours cannot be selected. In this section, we describe the data processing workflow utilized to obtain inverted V_S profiles. Specifically, we will demonstrate how the application of a frequency-wavenumber ($f-k$) filter to CCFs helps to mitigate spurious arrivals and enhance the quality of the CCFs.

3.2.1 Cross-correlation functions

The entire dataset is first downsampled to 40 Hz, then windowed into short time series, demeaned, and bandpass filtered between 0.01 - 20 Hz. We also apply a 1-bit normalization to reduce the influence of non-stationary sources (Bensen et al., 2007). We then use the cross-coherence approach to emphasize the phase information, which is more suitable for noisy data that vary in amplitude among traces or have long and complex source wavelets (Nakata et al., 2011). The CCFs from cross-coherence interferometry are computed in the frequency domain as follows:

$$CCF(x_{\mathrm{A}}, x_{\mathrm{B}}, \tau) = \left\langle \mathcal{F}^{-1}\left[\frac{s\left(x_{\mathrm{A}}, \omega\right) s^{*}\left(x_{\mathrm{B}}, \omega\right)}{\{|s\left(x_{\mathrm{A}}, \omega\right)|\}\{|s\left(x_{\mathrm{B}}, \omega\right)|\}}\right]\right\rangle; \tag{1}$$

where $s\left(x_{\mathrm{A}}, \omega\right)$ and $s\left(x_{\mathrm{B}}, \omega\right)$ are the Fourier transform of windowed strain rate recordings at the receiver channels x_{A} and x_{B}, respectively. The asterisk indicates a complex conjugate and $\{\cdot\}$ represents a smoothing of the absolute amplitude spectrum ($|\cdot|$) using a running absolute mean algorithm. The inverse Fourier transform ($\mathcal{F}^{-1}$) is applied to retrieve the CCFs in the time domain. $\langle\cdot\rangle$ expresses the stacking CCFs for all time windows. In general, the SNR increases by stacking over longer periods. However, since we only have 19 hours of data, we optimized the interval and overlap of CCF time windows. After testing parameters, CCFs are computed using 30-s windows with 50% overlap, and final CCFs are folded at zero time lag and stacked. In addition, we use the phase-weighted stacking method to further enhance the signal quality (Schimmel & Paulssen, 1997). CCFs are computed for virtual sources every five channels (i.e., every 24 m) with the corresponding 100 receiver channels (e.g., virtual source 610 with channels 610 to 710). These 100 CCFs form a virtual shot gather, which depicts the seismic wavefield propagating between the virtual source and the corresponding receivers (Fig. 2a). Finally, we only compute virtual shot gathers for straight sections of the fiber because we focus on Rayleigh wave (E. Martin et al., 2016).

3.2.2 Remove spurious arrival using $f-k$ filtering

We utilize the high spatial density of the DAS array to transform the time-domain virtual shot gathers $S\left(t,x\right)$ to its frequency-wavenumber ($f-k$) representation $\tilde{S}\left(\omega,k\right)$ (Fig. 2a & e, respectively). We then apply two filters to $\tilde{S}\left(\omega,k\right)$. The first one selects waves propagating in a certain velocity range (Embree et al., 1963) (Fig. 2b) and involves a phase velocity taper denoted by g:

$$\tilde{s}\left(\omega,k\right) = g\left(\omega,k,c_a,c_b,c_c,c_d\right) * \tilde{S}(\omega,k) \quad (2)$$

$$\text{with } g\left(\omega,k,c_a,c_b,c_c,c_d\right) = \begin{cases} \sin\frac{\pi}{2}\frac{c-c_a}{c_b-c_a}, & \text{if } c_a \le c \le c_b \\ 1, & \text{if } c_b < c < c_c \\ 1-\sin\frac{\pi}{2}\frac{c-c_c}{c_d-c_c}, & \text{if } c_c \le c \le c_d \\ 0, & \text{otherwise.} \end{cases} \quad (3)$$

Here $c = \omega/k$ is the observed phase velocity, and $c_b = 100$ m/s, $c_c = 2500$ m/s, and $c_a = 0.95c_b$ and $c_d = 1.05c_c$ are the velocity parameters of the taper. The virtual shot gather resulting from this first filter is shown in Figure 2b. The low-velocity waves already appear more clearly. On the basis of the first filter, the second filter further helps remove reflected waves, waves due to secondary sources, or aliasing, i.e. waves propagating in unexpected directions (Cheng et al., 2018). By noting the different quadrants of Fig.2e as Q1, Q2, Q3, and Q4, we observe the symmetry: $\|\tilde{S}\left(\omega,k\right)\| = \|\tilde{S}\left(-\omega,-k\right)\|$ and $\|\tilde{S}\left(-\omega,k\right)\| = \|\tilde{S}\left(\omega,-k\right)\|$, i.e Q1=Q3 and Q2=Q4. However, the absolute maximum amplitude (red and green lines) are all parallel, suggesting the effect of aliasing (D.-Y. Wang & Ling, 2016). By selecting only the quadrant Q2 (i.e. $\tilde{S}\left(\omega>0,k<0\right)$)

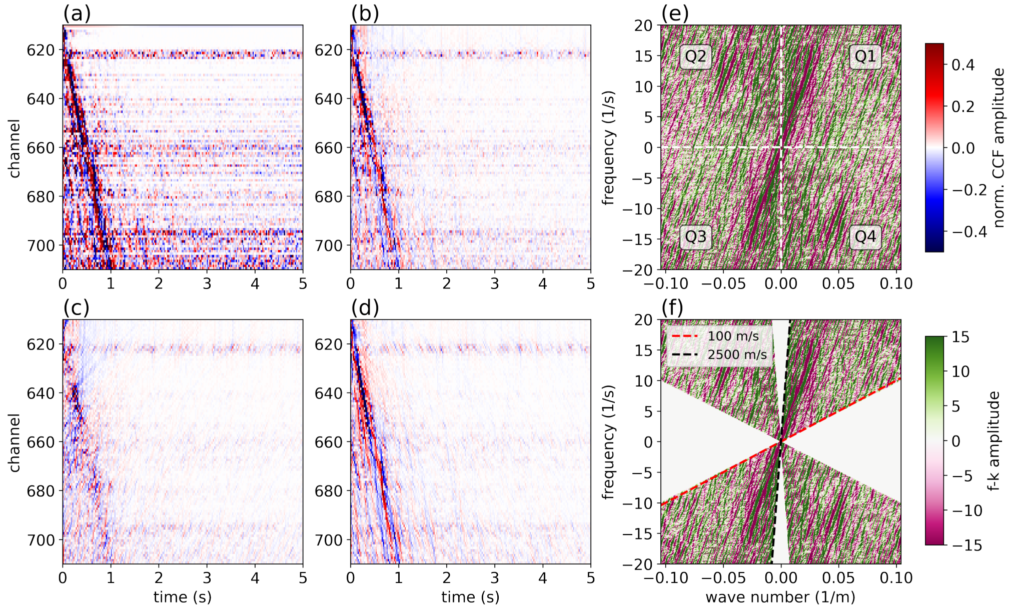

Figure 2. Virtual shot gather for channel #610 and the $f-k$ spectrum. (a) Initial virtual shot gather before $f-k$ filtering. (b) Virtual shot gather after a $f-k$ filtering, using the filter shown in f and following Eq. 2. (c) virtual shot gather using filtered $f-k$ spectrum but only using Q1 and Q3 after a phase velocity taper in (f). (d) Similar to (c) but using energy from Q2 and Q4.

after a phase velocity taper, to construct a fully symmetric $\tilde{S}$, we obtain the virtual shot gather shown in Figure 2c, where we mainly observe waves propagating toward the source. On the opposite, by constructing a fully symmetric $\tilde{S}$ from the unique selection of Q1, we retrieve surface waves propagating from the source (Fig. 2d). This process clearly improves the quality of the retrieved Rayleigh wave as well as the overall SNR of the filtered CCFs (Fig. 2d).

We also applied the $f-k$ filtering to raw DAS data to investigate if we could improve the SNR by removing moving sources. In particular, we focused on the locations exposed to vehicular traffic from two opposite directions (channels #3400-3600 located in western mountain areas). After filtering the waves outside the velocity range [5, 40] m/s, we enhance the passing of three cars by making apparent three straight lines (fig. S1b) and further selected wave propagating either in the positive or negative directions (fig. S1c, d). Even if waves propagating in one of the directions are entirely removed, the straight lines associated with the traffic do not completely disappear after $f-k$ filtering (fig. S1d). This is because cars are not only imposing stress changes where they pass but also continuously generate waves in both directions due to their acceleration or their contact with road asperities. Consequently, the effect of coherent sources present between the channels cannot be fully removed. Additionally, the efficacy of the filtering requires the optical fiber section to be straight and applied through time-limited windows. Then, using this process to raw data prior to signal correlation is computationally expensive and may not guarantee the removal of in-between source effects. As a result, we only applied the $f-k$ filtering directly to CCFs.

3.2.3 Phase velocity estimation

We then calculate the SNR as the energy ratio of the signal in the time window of expected wave arrivals, i.e., of $s(t)$ with $t \in [d/v_{max}, d/v_{min}]$ with $v_{max} = 2500$ m/s and $v_{min} = 100$ m/s, and the noise defined by $s(t)$ with $t > [d/v_{min}]$. We then apply a slant stack algorithm (Chapman, 1981) to the filtered CCFs with SNR larger than 10 to obtain dispersion images in the frequency-velocity domain (fig. S2). As observed in a previous study Viens et al. (2023), the number of receivers considered in the slant stack process impacts the retrieval of the dispersion curves (DCs, Fig. 3a, b & c). A higher number of receivers allows a better dispersion curve mode separation by sampling the wavefield with a smaller wave number interval. Yet, it afflicts spatial resolution. According to the tests shown in Fig. 3, we consider the number of 70 channels during the slant stack process at source 610 a good compromise. However, this number also depends on local conditions (e.g., the shape of the array). Therefore, we optimize it for all the sources and obtain numbers that range between 40 and 70 (Table 1). Next, we extract the dispersion points from the local energy maxima (energy maxima within subsets) observed in the dispersion images for each frequency (Fig. 3a). Nonetheless, to avoid artifacts at low velocity, we further impose a selection in the frequency-velocity domain, as shown in Fig. 3b, similarly to (Viens et al., 2023). Finally, we select nine sources at which the dispersion pictures allowed obtaining enough information to realize the inversion of the dispersion points, including one source in mountainous areas (see fig. S2). Table 1 displays the details of these virtual sources, including the number of receivers and the retrieved modes of dispersion.

3.2.4 V_S inversion

As explained in Viens et al. (2023), it is challenging to associate the selected dispersion points to a continuous curve for a given mode, particularly at high frequencies. Therefore, these points are treated individually without relating them to a specific mode and we minimize the distance between each of these dispersion points to the theoretical DCs. The forward theoretical DCs calculation follows the method presented in Perton & Sánchez-Sesma (2016). The distance is given

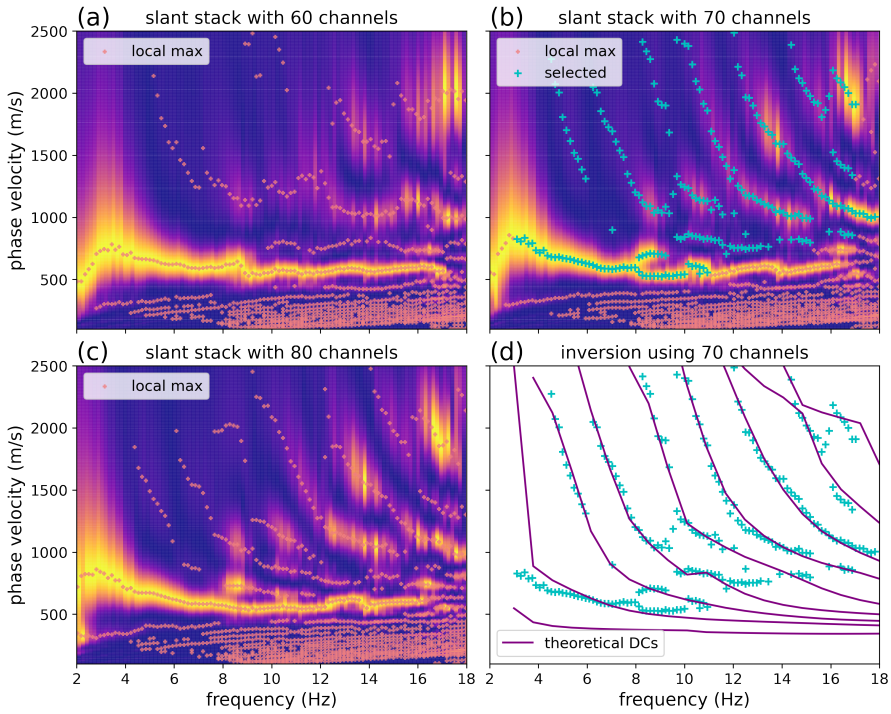

Figure 3. Slant slack and dispersion images using virtual shot gather obtained for channel #610 and shown in Fig. 2d. (a-c) show the normalized spectral energy with 60, 70, and 80 channels. (d) shows the observed and theoretical DCs computed from the inverted V_S model #610 (Fig. 4).

by the misfit function between the observed and theoretical Rayleigh wave phase velocities (Eq. 4):

$$\epsilon_{\mathrm{DC}}^2 = \frac{1}{J_{\max}} \sum_{f=f_{\min}}^{f_{\max}} \sum_{j=0}^{j_{\max}} \sum_{n=0}^{n_{\max}} G\left(\left|c_j^{\mathrm{obs}}(f) - c_n^{\mathrm{th}}(f)\right|\right)^2 \tag{4}$$

where c_j^{obs} and c_n^{th} are the phase velocities of the observed and theoretical dispersion curves, respectively. n represents the number of theoretical modes and j is the number of observed DC points at a certain frequency f. $J_{\max}$ is the number of selected DC points in the frequency band from $f_{\min}$ to $f_{\max}$. The function G evaluates if a selected dispersion point aligns with a theoretical dispersion point using the following equation:

$$G(x) = \begin{cases} x & \text{when} \quad |x| \leq \delta \\ \delta & \text{when} \quad |x| > \delta \end{cases} \tag{5}$$

where δ represents the misfit threshold which is set to the average velocity difference between the observed DC points. The misfit function is minimized by a constrained nonlinear optimization method (Byrd et al., 1999; Perton et al., 2020).

We start the inversion process with an initial V_S profile built from two previous velocity models. The shallow layers ($\leq$150 m) are similar to the ones presented inVidal et al. (2014), and the half-space ($\leq$400 m), which corresponds to the basement assessed in Chourak et al. (2003), has a velocity of $\sim$3 km/s. As surface wave DCs hold a higher sensitivity to V_S compared with density and the compression-wave velocity V_P (Yoshizawa & Kennett, 2005), these two latter parameters are determined from V_S by using the empirical relationships of (Brocher, 2005). Then, the inversion process has only two free parameters by layer: the thickness and V_S.

4 Results

We present the 1-D V_S models at different virtual sources in Figure 4. The velocity models allow identifying two main seismic horizons in the upper 160 m. The shallowest seismic horizon has a V_S ranging between $\sim$350 and $\sim$600 m/s, while the second horizon, identified as detritic rocks, has a mean V_S of 2500-3000 m/s. The shallow seismic horizon has a minimum thickness of about 90 m, which increases to 125-135 m for models #595, 605, and 610. The interface between these two seismic horizons has a significant V_S contrast, and the highest velocities for both horizons are observed at site #2850, on top of the Alhambra formation.

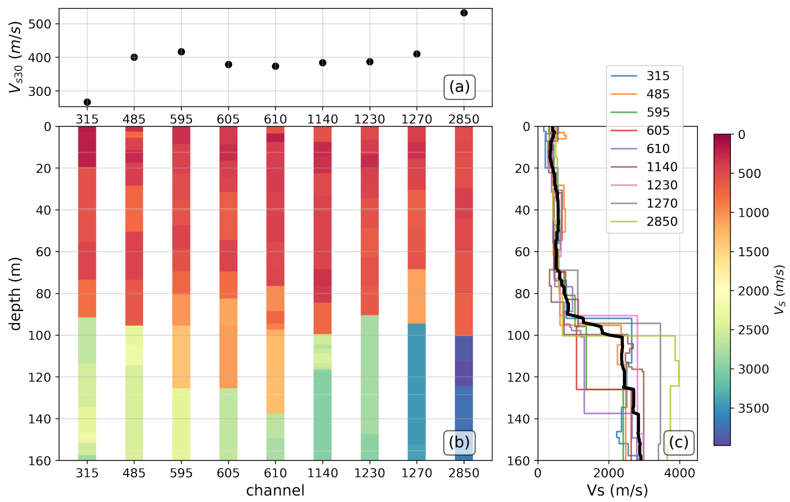

Figure 4. Shear-wave velocity inversion results. (a) V_{S30} for all inverted models. (b) 1-D V_S inversion results from all analyzed sections of the fiber cable. (c) All the inverted models in lines. The black line is the average of all velocity profiles.

To further investigate the shallow V_S properties, we extract the V_{S30} (average shear-wave velocity of the top 30-m depth). The variations in V_{S30} values across different virtual sources reflect the spatial heterogeneity of the subsurface. Our results reveal that the slowest V_{S30} of $\sim$270 m/s is found at site #315 in the heart of the city, while the fastest ($\sim$530 m/s) is located near site #2850, in the mountain. The V_{S30} values are relatively constant in other sections of the array and are around 400 m/s.

4.1 Reliability of the results

To establish the reliability of our results, we conduct a sensitivity analysis of the inversion method by examining the sensitivity kernel of each individual DC as well as the effect of all jointly inverted modes on the V_S models. The sensitivity kernels enable us to assess the sensitivity of each individual Rayleigh DC as a function of depth and frequency (Aki & Richards, 2002; Tanimoto & Tsuboi, 2009; Campman & Dwi Riyanti, 2007). For instance, a certain mode may show more sensitivity to shallow parts at high frequencies, while being more sensitive to deeper depths at lower frequencies. At a given frequency, higher modes of Rayleigh waves exhibit more sensitivity to the deeper V_S structure (fig. S3). Therefore, multi-mode DCs can offer more constraints to the deeper structure. The DCs exhibit the most sensitivities to the upper 100 m and moderate sensitivities to depths between $\sim$100 and $\sim$150 m (fig. S3). However, these sensitivity kernels

Sources	Receiver Numbers	Retrieved Modes	V_{S30} (m/s)
315	40	7	266
485	50	5	400
595	60	7	416
605	60	7	378
610	70	8	373
1140	60	7	384
1230	50	6	387
1270	50	4	410
2850	40	5	532

Table 1. Summary of virtual sources, number of receivers, retrieved modes, and corresponding V_{S30} values of each velocity model.

offer only partial information as they consider each mode independently, and the sensitivity might be higher by considering these kernels jointly. As discussed in Perton et al. (2022), the joint sensitivity is better assessed by presenting all the velocity models within twice the lowest misfit. We present these variations at virtual source #610 in fig. S4. In general, the shallowest regions ($\leq$75 m) show less uncertainty thanks to higher Rayleigh wave sensitivity. Yet, the first two layers in the upper 10 meters exhibit higher variability, suggesting a more complex superficial structure with likely more lateral variations. There is also a large velocity variability above the two seismic horizons interface, i.e. between 75-100 m depth.

Another approach to estimating the site characteristics is the horizontal-to-vertical spectral ratio computed from ASF, also known as the H/V method (Nakamura, 1989). Subsurface elastic property contrasts along depth can have a significant impact on the resonant frequency (represented by the H/V peak frequency), making H/V analysis highly sensitive to identifying the depth of the impedance contrasts. In addition, the H/V method has recently gained theoretical developments from the diffuse field theory as it corresponds to the horizontal-to-vertical energy densities ratio of the ASF (Perton et al., 2009; Sánchez-Sesma et al., 2011). To further validate our results, we compare the observed H/V from ASF data recorded at a nearby three-component accelerometer (EXCAB, Fig 1a) with the theoretical H/V computed from velocity profile #595. The observed H/V is calculated through the autocorrelation of the signal components as in Eq. 6 (Perton et al., 2018). The theoretical H/V calculation is made according to Eq. 7 and by using the Discrete Wave Number method to calculate the Green function components $G_{ii}(\omega)$ (Bouchon, 2003; Sánchez-Sesma et al., 2011):

$$\frac{H}{V}(\mathbf{x},\omega) = \sqrt{\frac{\left\langle |v_1(\mathbf{x},\omega)|^2 \right\rangle + \left\langle |v_2(\mathbf{x},\omega)|^2 \right\rangle}{\left\langle |v_3(\mathbf{x},\omega)|^2 \right\rangle}}; \tag{6}$$

$$= \sqrt{\frac{\mathrm{Im}\left(\mathcal{G}_{11}(\mathbf{x},\omega) + \mathcal{G}_{22}(\mathbf{x},\omega)\right)}{\mathrm{Im}\left(\mathcal{G}_{33},(\mathbf{x},\omega)\right)}} \tag{7}$$

where $v_i(\omega)$ is the particular velocity spectrum components, with $i \in \{1, 2\}$ corresponds to horizontal directions, and $i = 3$ refers to the vertical direction. $\langle\cdot\rangle$ represents the average over several windows. $G_{ii}(\omega)$ is the displacement in the direction i caused by a unit point force applied in the same direction. $Im()$ denotes the imaginary part operator.

To further enhance our understanding of the velocity contrast, a simplified two-layer model of V_S is designed. Figure 5 shows the results of the observed vs. the theoretical H/Vs, for the model at channel #595 and the simplified velocity structure. All the H/V curves exhibit a dominant peak with a frequency of 1-2 Hz and comparable amplitudes. By employing the simplified two-layer model, this peak amplitude can more easily be associated with the velocity contrast at a depth of approximately 80 m. Therefore, it confirms the reliability and reasonable constraints of the obtained interface depth and velocity contrast for the two main seismic horizons across multiple V_S models.

5 Discussion

5.1 Shallow structure under Granada city

Taken together, our results provide a seismic characterization of two main seismic horizons with a strong velocity contrast at depths greater than 90 m. At the west of the Alhambra fault in the urban area, the deeper horizon shows consistent and high V_S values ranging between $\sim$2300-3000 m/s, which is associated with Plio-Quaternary detritic rocks. In the mountainous region (model #2850), the velocities of this deeper seismic horizon jump to $\sim$3800 m/s, associated with the Late-Miocene detritic rocks and gypsum (Fig. 1c). According to Madarieta-Txurruka et al. (2021), it is expected that these geological units have similar thicknesses in the vicinity of profile A-A' (Fig. 1c).

The shallower seismic horizon (<80-100 m) shows comparable average velocities of around 500 m/s along the fiber. However, this seismic horizon is identified as Quaternary alluvial deposits

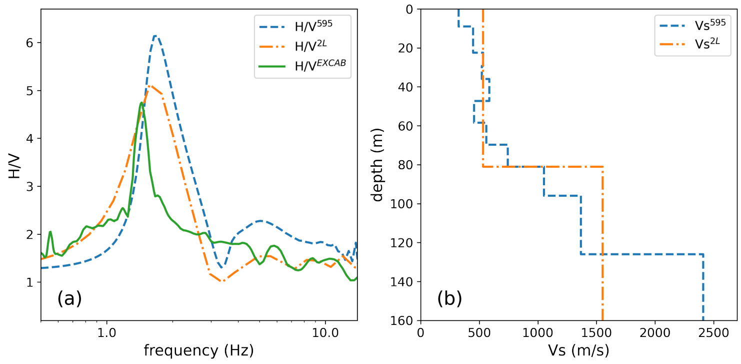

Figure 5. H/V Comparison and V_S models. (a) The green solid line depicts the H/V measurement from the accelerometer EXCAB. The dash and dash-dot lines are the theoretical H/V curves calculated from the inverted velocity model #595 and from a simplified two-layer model, respectively. (b) V_S models used to compute theoretical H/V shown in (a).

in the city area, and as the Alhambra formation conglomerates in the mountain area (Madarieta-Txurruka et al., 2021) (Fig. 1c). Although their different geological origins, it is difficult to distinguish them in our inversion results. Finally, on top of these seismic horizons, stand different kinds of soils (Fig. 1a).

As a typical index for soil conditions, V_{S30} is used for site classification in Uniform Building Code in the US (Dobry et al., 2000) and in the Eurocode 8 in Europe (Code, 2005; Kanlı et al., 2006). According to Spanish Seismic Code NCSE-02 (NCSE-02, 2002), soil types are classified under Type II and III with a V_{S30} range of 400-750 m/s and 200-400 m/s, respectively. Most inverted V_S models stand at the common limit of these two categories as they have V_{S30} between $\sim$370-415 m/s. Models #315 (V_{S30} = 266 m/s), and #2850 (V_{S30} = 532 m/s) are classified with less ambiguity as type III soil (i.e., medium-soft soil) and type II soil (i.e., medium-hard soil), respectively. Additionally, #315 and #485 are located on top of clayey soils that are composed of red clays, gravel, and sand (Fig. 1a, (Geological Survey of Spain, 2014)). Model #315 could reflect the soft clayey soils with a low V_{S30} value of 266 m/s. These values align with a study from Navarro et al. showing that V_{S30} for a site located in the urban area affected by the upper part of the Genil river alluvial fan is $\sim$294 m/s. Besides, model #485 results from several receivers overlapping with the floodplain region. This may explain why this model has slightly higher velocities even though it is located on clayey soils in Fig. 1a. Overall, other areas on top of the floodplain region, which comprise sands, gravels, and carbonates, have typical V_{S30} values around 400 m/s. Finally, model #2850 is close to alluvium with compact conglomerates, which show higher V_{S30} (i.e., ∼530 m/s) than clayey soils, comparable to V_{S30} observed on Alhambra formation (Navarro et al., 2010; Vidal et al., 2014).

However, the sensitivity of inversion shows a larger uncertainty for the shallowest 10 m (fig. S4) due to the intricate heterogeneous and complex nature of the urban shallow subsoil that may be compacted, stiffened by constructions, or crossed by human infrastructure (tunnels, pipes etc.). Due to this possible lack of resolution in the V_{S30}, it is preferable to discuss the general features of the velocity models. In addition, the V_{S30} values only provide a first-order approximation for liquefaction hazard and for estimating site amplification factors by considering a standard velocity at the basement (Borcherdt, 2012). However, as observed with the H/V measurements, elastic resonances of surface waves may change the amplification behavior at a specific frequency due to strong contrast at depth. For seismic hazard assessment, it is important that these frequencies do not correspond to the building's vibration frequency which depends roughly on their height. The velocity profiles demonstrate a high impedance contrast at a depth of 90-140 m (Fig. 4) and H/V peak frequencies ranging from 1-2 Hz (Fig. 5), as observed by Vidal et al. (2014) and Vidal & Feriche (2012). Therefore, this area is likely inadequate for tall buildings of about 10 stories that could vibrate with the soil's dominant frequency.

5.2 Challenges of extracting surface wave information

The utilization of DAS provides a promising non-invasive method for conducting dense seismic measurements in urban areas. However, despite the GranaDAS array consisting of 4167 channels, we were able to obtain high-quality dispersion images at only nine locations along the cable. Several reasons can explain the limited number of observations using an urban telecom fiber. For instance, DAS data are affected by the often unknown and uneven cable-ground coupling, which can reduce sensitivity to ground motion and cause several cable segments unsuitable for seismic measurements (e.g., Ajo-Franklin et al., 2019; Yuan et al., 2020; Z. J. Spica et al., 2020; Tribaldos et al., 2021). As each cable has its own set of characteristics, the coupling should therefore be one of the first parameters assessed for seismological studies.

Low coupling regions can result in low-SNR CCFs and make it challenging to extract surface wave information. Nonetheless, the SNR can increase with longer time series stacking (Bensen et al., 2007). In Granada, we only recorded strain rate during 19 hours and during day time. Such a short recording duration may hinder the Green's function retrieval, especially at lower frequencies where ASF tends to be less coherent.

In addition, the crooked layout of the GranaDAS array in urban areas can pose further challenges for extracting surface wave information. Indeed, computing CCFs along winding sections of the fiber can result in the emergence of a combination of Love and Rayleigh waves (E. R. Martin et al., 2021), making it difficult to separate both wavefields (Song et al., 2021). Typically, pure Rayleigh waves are obtained through radial-radial cross-correlations, limiting their retrieval to straight subsections of the fiber. This physical requirement further restricts the areas where we can assess the subsurface information (e.g., Shragge et al., 2021; Rodríguez Tribaldos & Ajo-Franklin, 2021; Yang et al., 2022; Song et al., 2021).

Despite the combined challenges of coupling, short-duration recordings, and twisting array geometry, DAS also offers unique opportunities to improve the resolution of the dispersion images. For example, it is a common problem in seismology to acquire high-quality multi-mode DCs (Z. Spica et al., 2017; Perton et al., 2020; Viens et al., 2023; Takagi & Nishida, 2022). In this case, one advantage of using DAS for ASF interferometry is the ability to adjust the number of receivers and channel spacing during the processing steps, improving modal content and avoiding wavefield aliasing for a given virtual source (Viens et al., 2023). During our processing, we adjust these parameters to improve the quality of the modal content (Table 1). Ultimately, we obtain Rayleigh wave DCs with up to eight modes, providing more resolution to our models.

6 Conclusions

We present a case study to image the detailed shallow V_S structure (< 160 m) in the city of Granada using a DAS acquisition on a telecommunication fiber cable. We process 19-h ASF data using the cross-coherence correlation interferometric method to generate virtual shot gathers along the fiber. We apply an ad-hoc $f - k$ filter to remove waves propagating in unexpected and spurious directions, which improves the quality of the CCFs. Then, we convert the CCFs into dispersion diagrams by applying the slant stack technique. Despite the challenges of using telecommunication fiber in an urban area, we are able to generate several dispersion images that exhibit rich multi-mode Rayleigh wave energy within the frequency range of 2-18 Hz. Finally, we invert Rayleigh wave dispersion points into 1-D V_S models using a global optimization algorithm and image the top 160-m V_S structure. V_S profiles suggest softer structures for the site on clayey soils and stiffer structures for the site with conglomerates near the mountain areas. Our results show that the shallow alluvial deposits and detritic rocks have V_S values of $\sim$300-600 m/s and $\sim$2500-3000 m/s, respectively. The interface of these two units is generally located at depths of $\sim$100 m, while it is slightly deeper for sites with older alluvium. This study highlights the potential of utilizing ASF data obtained through urban DAS for near-surface characterization, notwithstanding the associated difficulties. The extensive sensor network provided by DAS makes it a promising tool for seismic microzonation, which is a crucial aspect of seismic risk analysis in densely populated urban areas.

Acknowledgments

Most of the figures are plotted with Matplotlib (Hunter, 2007), and some of the data processing steps have been performed using ObsPy (Beyreuther et al., 2010). **Funding:** Y.L. is supported by NSF award EAR2022716 and M.P. is supported by CONACyT award CF-2019-G-6655. Z.J.S. acknowledges support from the Air Force Research Laboratory grant FA9453-21-2-0018. **Competing interests:** The authors declare that they have no competing interests.

DATA AVAILABILITY

All the GranaDAS array data will be available on PubDAS (Z. J. Spica et al., 2023) after revision and prior potential acceptance of this article. Accelerometer data can be accessed upon request to the National Geographic Institute of Spain. The velocity models at all sites are available at GitHub.

References

Ajo-Franklin, J. B., Dou, S., Lindsey, N. J., Monga, I., Tracy, C., Robertson, M., … others (2019). Distributed acoustic sensing using dark fiber for near-surface characterization and broadband seismic event detection. *Scientific reports*, *9*(1), 1–14.

Aki, K. (1993). Local site effects on weak and strong ground motion. *Tectonophysics*, *218*(1-3), 93–111.

Aki, K. (1998, Jun). Local site effects on strong ground motion. In *Earthquake engineering and soil dynamics ii-recent advances in ground motion evaluation.* Park City, Utah.

Aki, K., & Richards, P. (2002). *Quantitative Seismology*. University Science Books.

Banda, E., & Ansorge, J. (1980). Crustal structure under the central and eastern part of the betic cordillera. *Geophysical Journal International*, *63*(2), 515–532.

Bensen, G., Ritzwoller, M., Barmin, M., Levshin, A. L., Lin, F., Moschetti, M., … Yang, Y. (2007). Processing seismic ambient noise data to obtain reliable broad-band surface wave dispersion measurements. *Geophysical journal international*, *169*(3), 1239–1260.

Beyreuther, M., Barsch, R., Krischer, L., Megies, T., Behr, Y., & Wassermann, J. (2010). Obspy: A python toolbox for seismology. *Seismological Research Letters*, *81*(3), 530–533.

Biondi, E., Wang, X., Williams, E. F., & Zhan, Z. (2023). Geolocalization of large-scale das channels using a gps-tracked moving vehicle. *Seismological Society of America*, *94*(1), 318–330.

Bommer, C., Heesemann, E., Sagalova, V., Manne-Goehler, J., Atun, R., Bärnighausen, T., & Vollmer, S. (2017). The global economic burden of diabetes in adults aged 20–79 years: a cost-of-illness study. *Lancet Diabetes Endocrinol*, *5*(6), 423–430.

Bonnefoy-Claudet, S., Cotton, F., & Bard, P.-Y. (2006). The nature of noise wavefield and its applications for site effects studies: A literature review. *Earth-Science Reviews*, *79*(3-4), 205–227.

Borcherdt, R. D. (2012). Vs30–a site-characterization parameter for use in building codes, simplified earthquake resistant design, gmpes, and shakemaps. In *The 15th world conference on earthquake engineering.*

Bouchon, M. (2003). A review of the discrete wavenumber method. *Pure and applied Geophysics*, *160*, 445–465.

Brissaud, Q., Bowden, D. C., & Tsai, V. C. (2020). Extension of the basin rayleigh-wave amplification theory to include basin-edge effects. *Bulletin of the Seismological Society of America*, *110*(3), 1305–1322.

Brocher, T. M. (2005). Empirical relations between elastic wavespeeds and density in the earth's crust. *Bulletin of the seismological Society of America*, *95*(6), 2081–2092.

Buforn, E., Pro, C., Cesca, S., Udías, A., & Del Fresno, C. (2011). The 2010 granada, spain, deep earthquake. *Bulletin of the Seismological Society of America*, *101*(5), 2418–2430.

Buforn, E., Udias, A., & Madariaga, R. (1991). Intermediate and deep earthquakes in spain. In *Source mechanism and seismotectonics* (pp. 375–393). Springer.

Byrd, R. H., Hribar, M. E., & Nocedal, J. (1999). An interior point algorithm for large-scale nonlinear programming. *SIAM Journal on Optimization*, *9*(4), 877–900.

Campillo, M., Gariel, J., Aki, K., & Sanchez-Sesma, F. (1989). Destructive strong ground motion in mexico city: Source, path, and site effects during great 1985 michoacán earthquake. *Bulletin of the Seismological Society of America*, *79*(6), 1718–1735.

Campman, X., & Dwi Riyanti, C. (2007). Non-linear inversion of scattered seismic surface waves. *Geophysical Journal International*, *171*(3), 1118–1125.

Castellanos, J. C., & Clayton, R. W. (2021). The fine-scale structure of long beach, california, and its impact on ground motion acceleration. *Journal of Geophysical Research:*

Solid Earth, *126*(12), e2021JB022462.

Chapman, C. (1981). Generalized radon transforms and slant stacks. *Geophysical Journal International*, *66*(2), 445–453.

Cheng, F., Xia, J., Xu, Z., Hu, Y., & Mi, B. (2018). Frequency–wavenumber (fk)-based data selection in high-frequency passive surface wave survey. *Surveys in Geophysics*, *39*, 661–682.

Chourak, M., Corchete, V., Badal, J., Serón, F., & Gómez, F. (2003). Imaging of the near-surface shear-wave velocity structure of the granada basin (southern spain). *Bulletin of the Seismological Society of America*, *93*(1), 430–442.

Chung, W.-Y., & Kanamori, H. (1976). Source process and tectonic implications of the spanish deep-focus earthquake of march 29, 1954. *Physics of the Earth and Planetary Interiors*, *13*(2), 85–96.

Code, P. (2005). Eurocode 8: Design of structures for earthquake resistance-part 1: general rules, seismic actions and rules for buildings. *Brussels: European Committee for Standardization*.

Cruz-Atienza, V. M., Tago, J., Sanabria-Gómez, J., Chaljub, E., Etienne, V., Virieux, J., & Quintanar, L. (2016). Long duration of ground motion in the paradigmatic valley of mexico. *Scientific reports*, *6*(1), 1–9.

Dobry, R., Borcherdt, R., Crouse, C., Idriss, I., Joyner, W., Martin, G. R., … Seed, R. (2000). New site coefficients and site classification system used in recent building seismic code provisions. *Earthquake spectra*, *16*(1), 41–67.

Dou, S., Lindsey, N., Wagner, A. M., Daley, T. M., Freifeld, B., Robertson, M., … Ajo-Franklin, J. B. (2017). Distributed acoustic sensing for seismic monitoring of the near surface: A traffic-noise interferometry case study. *Scientific reports*, *7*(1), 1–12.

Embree, P., Burg, J. P., & Backus, M. M. (1963). Wide-band velocity filtering; the pie-slice process. *Geophysics*, *28*(6), 948–974.

Fang, G., Li, Y. E., Zhao, Y., & Martin, E. R. (2020). Urban near-surface seismic monitoring using distributed acoustic sensing. *Geophysical Research Letters*, *47*(6), e2019GL086115.

Galetzka, J., Melgar, D., Genrich, J. F., Geng, J., Owen, S., Lindsey, E. O., … others (2015). Slip pulse and resonance of the kathmandu basin during the 2015 gorkha earthquake, nepal. *Science*, *349*(6252), 1091–1095.

García-Dueñas, V., & Balanyá, J. (1986). Estructura y naturaleza del arco de gibraltar.

Maleo-Bol. Inf. Soc. Geol., Portugal, *2*, 23.

García-García, J., Vidal, F., Romacho, M., Martín-Marfil, J., Posadas, A., & Luzón, F. (1996). Seismic source parameters for microearthquakes of the granada basin (southern spain). *Tectonophysics*, *261*(1-3), 51–66.

Geological Survey of Spain. (2014). *Geode - continuous digital geological map of spain, scale 1:50.000.* `https://info.igme.es/cartografiadigital/geologica/Geode.aspx`.

Gil-Zepeda, S. A., Luzón, F., Aguirre, J., Morales, J., Sánchez-Sesma, F. J., & Ortiz-Alemán, C. (2002). 3d seismic response of the deep basement structure of the granada basin (southern spain). *Bulletin of the Seismological Society of America*, *92*(6), 2163–2176.

Grattan, K., & Sun, T. (2000). Fiber optic sensor technology: an overview. *Sensors and Actuators A: Physical*, *82*(1-3), 40–61.

Grimison, N. L., & Chen, W.-P. (1986). The azores-gibraltar plate boundary: Focal mechanisms, depths of earthquakes, and their tectonic implications. *Journal of Geophysical Research: Solid Earth*, *91*(B2), 2029–2047.

Gurria, E., Mezcua, J., Blanco, M. J., et al. (1997). Crustal and upper mantle velocity structure of southern iberia, the sea of alboran, and the gibraltar arc determined by local earthquake tomography.

Hamdache, M. (1998). Seismic hazard assessment for the main seismogenic zones in north algeria. *pure and applied geophysics*, *152*(2), 281–314.

Hartog, A. H. (2017). *An introduction to distributed optical fibre sensors*. CRC press.

Hubbard, P. G., Xu, J., Zhang, S., Dejong, M., Luo, L., Soga, K., … others (2021). Dynamic structural health monitoring of a model wind turbine tower using distributed acoustic sensing (das). *Journal of Civil Structural Health Monitoring*, *11*(3), 833–849.

Hunter, J. D. (2007). Matplotlib: A 2d graphics environment. *Computing in science & engineering*, *9*(03), 90–95.

Huot, F., Martin, E. R., & Biondi, B. (2018). Automated ambient noise processing applied to fiber optic seismic acquisition (das). In *Seg technical program expanded abstracts 2018* (pp. 4688–4692). Society of Exploration Geophysicists.

Jakkampudi, S., Shen, J., Li, W., Dev, A., Zhu, T., & Martin, E. R. (2020). Footstep detection in urban seismic data with a convolutional neural network. *The Leading Edge*, *39*(9), 654–660.

Jousset, P., Reinsch, T., Ryberg, T., Blanck, H., Clarke, A., Aghayev, R., … Krawczyk,

C. M. (2018). Dynamic strain determination using fibre-optic cables allows imaging of seismological and structural features. *Nature communications*, *9*(1), 1–11.

Kanlı, A. I., Tildy, P., Prónay, Z., Pınar, A., & Hermann, L. (2006). Vs 30 mapping and soil classification for seismic site effect evaluation in dinar region, sw turkey. *Geophysical Journal International*, *165*(1), 223–235.

Lee, S.-J., Chen, H.-W., Liu, Q., Komatitsch, D., Huang, B.-S., & Tromp, J. (2008). Three-dimensional simulations of seismic-wave propagation in the taipei basin with realistic topography based upon the spectral-element method. *Bulletin of the Seismological Society of America*, *98*(1), 253–264.

Lellouch, A., Yuan, S., Spica, Z., Biondi, B., & Ellsworth, W. (2019). Seismic velocity estimation using passive downhole distributed acoustic sensing records: Examples from the san andreas fault observatory at depth. *Journal of Geophysical Research: Solid Earth*, *124*(7), 6931–6948.

Lindsey, N. J., Martin, E. R., Dreger, D. S., Freifeld, B., Cole, S., James, S. R., … Ajo-Franklin, J. B. (2017). Fiber-optic network observations of earthquake wavefields. *Geophysical Research Letters*, *44*(23), 11–792.

Lindsey, N. J., Rademacher, H., & Ajo-Franklin, J. B. (2020). On the broadband instrument response of fiber-optic das arrays. *Journal of Geophysical Research: Solid Earth*, *125*(2), e2019JB018145.

Lindsey, N. J., Yuan, S., Lellouch, A., Gualtieri, L., Lecocq, T., & Biondi, B. (2020). City-scale dark fiber das measurements of infrastructure use during the covid-19 pandemic. *Geophysical research letters*, *47*(16), e2020GL089931.

Lozano, L., Cantavella, J. V., Gaite, B., Ruiz-Barajas, S., Antón, R., & Barco, J. (2022). Seismic analysis of the 2020–2021 santa fe seismic sequence in the granada basin, spain: Relocations and focal mechanisms. *Seismological Society of America*, *93*(6), 3246–3265.

Madarieta-Txurruka, A., Galindo-Zaldívar, J., González-Castillo, L., Peláez, J. A., Ruiz-Armenteros, A. M., Henares, J., … Gil, A. J. (2021). High-and low-angle normal fault activity in a collisional orogen: The northeastern Granada Basin (Betic Cordillera). *Tectonics*, *40*(7), e2021TC006715.

Martin, E., Lindsey, N., Dou, S., Ajo-Franklin, J., Daley, T., Freifeld, B., … Bjella, K. (2016). Interferometry of a roadside das array in fairbanks, ak. In *2016 seg international exposition and annual meeting.*

Martin, E. R. (2018). *Passive imaging and characterization of the subsurface with dis-*

tributed acoustic sensing (Unpublished doctoral dissertation). Department of Geophysics, Stanford University.

Martin, E. R., Castillo, C. M., Cole, S., Sawasdee, P. S., Yuan, S., Clapp, R., … Biondi, B. L. (2017). Seismic monitoring leveraging existing telecom infrastructure at the sdasa: Active, passive, and ambient-noise analysis. *The Leading Edge*, *36*(12), 1025–1031.

Martin, E. R., Huot, F., Ma, Y., Cieplicki, R., Cole, S., Karrenbach, M., & Biondi, B. L. (2018). A seismic shift in scalable acquisition demands new processing: Fiber-optic seismic signal retrieval in urban areas with unsupervised learning for coherent noise removal. *IEEE Signal Processing Magazine*, *35*(2), 31–40.

Martin, E. R., Lindsey, N. J., Ajo-Franklin, J. B., & Biondi, B. L. (2021). Introduction to interferometry of fiber-optic strain measurements. *Distributed Acoustic Sensing in Geophysics: Methods and Applications*, 111–129.

Montilla, J. A. P., de Galdeano, C. S., & Casado, C. L. (2003). Use of active fault data versus seismicity data in the evaluation of seismic hazard in the granada basin (southern spain). *Bulletin of the Seismological Society of America*, *93*(4), 1670–1678.

Montilla, J. P., de Galdeano, C. S., & Casado, C. L. (2001). Seismic potential of faults in the granada basin (betic cordillera, spain). *Bulletin of the Geological Society of Greece*, *34*(4), 1595–1600.

Morales, J., Seo, K., Samano, T., Pena, J. A., Ibanez, J. M., & Vidal, F. (1993). Site response on seismic motion in the granada basin (southern spain) based on microtremor measurements. *Journal of Physics of the Earth*, *41*(4), 221–238.

Morales, J., Serrano, I., Vidal, F., & Torcal, F. (1997). The depth of the earthquake activity in the central betics (southern spain). *Geophysical Research Letters*, *24*(24), 3289–3292.

Morales, J., Singh, S., & Ordaz, M. (1996). Analysis of the granada (spain) earthquake of 24 june, 1984 (m= 5) with emphasis on seismic hazard in the granada basin. *Tectonophysics*, *257*(2-4), 253–263.

Morales, J., Vidal, F., De Miguel, F., Alguacil, G., Posadas, A., Ibáñez, J., … Guirao, J. (1990). Basement structure of the granada basin, betic cordilleras, southern spain. *Tectonophysics*, *177*(4), 337–348.

Morales, J., Vidal, F., Pena, J., Alguacil, G., & Ibanez, J. (1991). Microtremor study in the sediment-filled basin of zafarraya, granada (southern spain). *Bulletin of the Seismological Society of America*, *81*(2), 687–693.

Muñoz, D., Cisternas, A., Udıas, A., Mezcua, J., De Galdeano, C. S., Morales, J., … others (2002). Microseismicity and tectonics in the granada basin (spain). *Tectonophysics*, *356*(4), 233–252.

Muñoz, D., & Udias, A. (1992). Earthquake occurrence and seismic zonation in south spain. In *Proceedings of the world conference on earthquake engineering, madrid, spain* (pp. 483–487).

Nakamura, Y. (1989). A method for dynamic characteristics estimation of subsurface using microtremor on the ground surface. *Railway Technical Research Institute, Quarterly Reports*, *30*(1).

Nakata, N., Snieder, R., Tsuji, T., Larner, K., & Matsuoka, T. (2011). Shear wave imaging from traffic noise using seismic interferometry by cross-coherence. *Geophysics*, *76*(6), SA97–SA106.

Narayan, J. P., & Singh, S. (2006). Effects of soil layering on the characteristics of basin-edge induced surface waves and differential ground motion. *Journal of earthquake engineering*, *10*(4), 595–614.

Navarro, M., Feriche, M., García-Jerez, A., Vidal, F., & Enomoto, T. (2010, February). Local site effects in granada town (southern spain) based on array microtremor measurements. In *International workshop on seismic microzoning and risk reduction.* Cuernavaca, Mexico.

NCSE-02. (2002). *Norma de construcción sismo-resistente: parte general y edificación (ncse-02).* Ministerio de Fomento Madrid.

Parker, L., Thurber, C., Zeng, X., Li, P., Lord, N., Fratta, D., … others (2018). Active-source seismic tomography at the brady geothermal field, nevada, with dense nodal and fiber-optic seismic arrays. *Seismological Research Letters*, *89*(5), 1629–1640.

Perton, M., Hernández, L. M., Figueroa-Soto, A., Sosa-Ceballos, G., Amador, J. D. J., Angulo, J., & Calò, M. (2022). The magmatic plumbing system of the acoculco volcanic complex (mexico) revealed by ambient noise tomography. *Journal of Volcanology and Geothermal Research*, *432*, 107704.

Perton, M., Sánchez-Sesma, F., Rodríguez-Castellanos, A., Campillo, M., & Weaver, R. (2009). Two perspectives on equipartition in diffuse elastic fields in three dimensions. *The Journal of the Acoustical Society of America*, *126*(3), 1125–1130.

Perton, M., & Sánchez-Sesma, F. J. (2016). Green's function calculation from equipartition theorem. *The Journal of the Acoustical Society of America*, *140*(2), 1309–1318.

Perton, M., Spica, Z., & Caudron, C. (2018). Inversion of the horizontal-to-vertical spectral ratio in presence of strong lateral heterogeneity. *Geophysical journal international*, *212*(2), 930–941.

Perton, M., Spica, Z. J., Clayton, R. W., & Beroza, G. C. (2020). Shear wave structure of a transect of the los angeles basin from multimode surface waves and h/v spectral ratio analysis. *Geophysical Journal International*, *220*(1), 415–427.

Pitarka, A., Irikura, K., Iwata, T., & Sekiguchi, H. (1998). Three-dimensional simulation of the near-fault ground motion for the 1995 hyogo-ken nanbu (kobe), japan, earthquake. *Bulletin of the Seismological Society of America*, *88*(2), 428–440.

Retailleau, L., & Beroza, G. C. (2021). Towards structural imaging using seismic ambient field correlation artefacts. *Geophysical Journal International*, *225*(2), 1453–1465.

Rodríguez-Fernández, J., & De Galdeano, C. S. (2006). Late orogenic intramontane basin development: the granada basin, betics (southern spain). *Basin research*, *18*(1), 85–102.

Rodríguez Tribaldos, V., & Ajo-Franklin, J. B. (2021). Aquifer monitoring using ambient seismic noise recorded with distributed acoustic sensing (das) deployed on dark fiber. *Journal of Geophysical Research: Solid Earth*, *126*(4), e2020JB021004.

Sánchez, F. V. (1987). *Sismotectónica de la region béticas-mar de alborán* (Unpublished doctoral dissertation). Universidad de Granada.

Sanchez-Sesma, F. J. (1987). Site effects on strong ground motion. *Soil Dynamics and Earthquake Engineering*, *6*(2), 124–132.

Sánchez-Sesma, F. J., Rodríguez, M., Iturrarán-Viveros, U., Luzón, F., Campillo, M., Margerin, L., … Rodriguez-Castellanos, A. (2011). A theory for microtremor h/v spectral ratio: application for a layered medium. *Geophysical Journal International*, *186*(1), 221–225.

Sanz de Galdeano, C., Peláez Montilla, J. A., & López Casado, C. (2003). Seismic potential of the main active faults in the granada basin (southern spain). *Pure and Applied Geophysics*, *160*(8), 1537–1556.

Schimmel, M., & Paulssen, H. (1997). Noise reduction and detection of weak, coherent signals through phase-weighted stacks. *Geophysical Journal International*, *130*(2), 497–505.

Semblat, J. F., Kham, M., Parara, E., Bard, P.-Y., Pitilakis, K., Makra, K., & Raptakis, D. (2005). Seismic wave amplification: Basin geometry vs soil layering. *Soil dynamics and earthquake engineering*, *25*(7-10), 529–538.

Serrano, I., Zhao, D., & Morales, J. (2002). 3-d crustal structure of the extensional granada basin in the convergent boundary between the eurasian and african plates. *Tectonophysics*, *344*(1-2), 61–79.

Shragge, J., Yang, J., Issa, N., Roelens, M., Dentith, M., & Schediwy, S. (2021). Low-frequency ambient distributed acoustic sensing (das): case study from perth, australia. *Geophysical Journal International*, *226*(1), 564–581.

Snieder, R., Fan, Y., Slob, E., & Wapenaar, K. (2010). Equipartitioning is not sufficient for green's function extraction. *Earthquake Science*, *23*, 403–415.

Song, Z., Zeng, X., & Thurber, C. H. (2021). Surface-wave dispersion spectrum inversion method applied to love and rayleigh waves recorded by distributed acoustic sensing. *Geophysics*, *86*(1), EN1–EN12.

Spica, Z., Perton, M., & Legrand, D. (2017). Anatomy of the colima volcano magmatic system, mexico. *Earth and Planetary Science Letters*, *459*, 1–13.

Spica, Z. J., Ajo-Franklin, J., Beroza, G. C., Biondi, B., Cheng, F., Gaite, B., … others (2023). Pubdas: A public distributed acoustic sensing datasets repository for geosciences. *Seismological Society of America*.

Spica, Z. J., Perton, M., Martin, E. R., Beroza, G. C., & Biondi, B. (2020). Urban seismic site characterization by fiber-optic seismology. *Journal of Geophysical Research: Solid Earth*, *125*(3), e2019JB018656.

Stich, D., Batlló, J., Morales, J., Macià, R., & Dineva, S. (2003). Source parameters of the mw= 6.1 1910 adra earthquake (southern spain). *Geophysical Journal International*, *155*(2), 539–546.

Takagi, R., & Nishida, K. (2022). Multimode dispersion measurement of surface waves extracted by multicomponent ambient noise cross-correlation functions. *Geophysical Journal International*, *231*(2), 1196–1220.

Tanimoto, T., & Tsuboi, S. (2009). Variational principle for rayleigh wave ellipticity. *Geophysical Journal International*, *179*(3), 1658–1668.

Tribaldos, V. R., Ajo-Franklin, J. B., Dou, S., Lindsey, N. J., Ulrich, C., Robertson, M., … Tracy, C. (2021). Surface wave imaging using distributed acoustic sensing deployed on dark fiber: Moving beyond high-frequency noise. *Distributed Acoustic Sensing in Geophysics: Methods and Applications*, 197–212.

Vidal, F., Alguacil, G., Navarro, M., Valverde, I., García-Jerez, A., García-Villena, F., & Enomoto, T. (2014, August). Simulation of earthquake ground motion in granada city (spain). In *Second european conference on earthquake engineering and seismology.* Istanbul, Turkey.

Vidal, F., & Castillo, G. D. (1994). Granada facing an earthquake. In *Issues in urban earth-*

quake risk (pp. 291–300). Springer.

Vidal, F., & Feriche, M. (2012, September). Site response estimation at granada city (southern spain) based on records of a deep earthquake. In *15th world conference on earthquake engineering.* Lisbon, Portugal.

Viens, L., Bonilla, L. F., Spica, Z. J., Nishida, K., Yamada, T., & Shinohara, M. (2022). Nonlinear earthquake response of marine sediments with distributed acoustic sensing. *Geophysical Research Letters*, *49*(21), e2022GL100122. doi: 10.1029/2022GL100122

Viens, L., Perton, M., Spica, Z. J., Nishida, K., Yamada, T., & Shinohara, M. (2023). Understanding surface wave modal content for high-resolution imaging of submarine sediments with distributed acoustic sensing. *Geophysical Journal International*, *232*(3), 1668–1683.

Wang, D.-Y., & Ling, Y. (2016). Phase-shift-and phase-filtering-based surface-wave suppression method. *Applied Geophysics*, *13*(4), 614–620.

Wang, X., Williams, E. F., Karrenbach, M., Herráez, M. G., Martins, H. F., & Zhan, Z. (2020). Rose parade seismology: Signatures of floats and bands on optical fiber. *Seismological Research Letters*, *91*(4), 2395–2398.

Yang, Y., Atterholt, J. W., Shen, Z., Muir, J. B., Williams, E. F., & Zhan, Z. (2022). Sub-kilometer correlation between near-surface structure and ground motion measured with distributed acoustic sensing. *Geophysical Research Letters*, *49*(1), e2021GL096503.

Yoshizawa, K., & Kennett, B. (2005). Sensitivity kernels for finite-frequency surface waves. *Geophysical Journal International*, *162*(3), 910–926.

Yuan, S., Lellouch, A., Clapp, R. G., & Biondi, B. (2020). Near-surface characterization using a roadside distributed acoustic sensing array. *The Leading Edge*, *39*(9), 646–653.

Zeng, X., Lancelle, C., Thurber, C., Fratta, D., Wang, H., Lord, N., … Clarke, A. (2017). Properties of noise cross-correlation functions obtained from a distributed acoustic sensing array at garner valley, california. *Bulletin of the Seismological Society of America*, *107*(2), 603–610.

Zhu, T., & Stensrud, D. J. (2019). Characterizing thunder-induced ground motions using fiber-optic distributed acoustic sensing array. *Journal of Geophysical Research: Atmospheres*, *124*(23), 12810–12823.